16TH EUROPEAN CONFERENCE ON EARTHQUAKE ENGINEERING THESSALONIKI 18 - 21 JUNE 2018

A MATERIAL POINT METHOD FOR STUDYING ROCKING SYSTEMS

Emmanouil G. Kakouris[1], Manolis N. Chatzis[2], Savvas P. Triantafyllou[3]

ABSTRACT

In this work, a Material Point Method (MPM) is employed for the analysis of rocking body dynamics. MPM is effectively an Arbitrary Lagrangian Eulerian scheme where the continuum is represented by a set of material points that are moving within a fixed computational grid; solution of the governing equations is performed in this grid considering an appropriate mapping. To accurately account for the contact dynamics between the bodies, a discrete field approach is adopted whereby each deformable domain is treated independently whereas impenetrability constraints and a Coulomb friction model are introduced to account for the contact at the interface. The proposed scheme is used to simulate the rocking response of a rigid body on an elastic-half space and comparisons are made with the Inverted Pendulum and Winkler rocking models.

Keywords: Rocking mechanics; Contact mechanics; Material Point Method.

1. INTRODUCTION

Rocking dynamics occur in systems whose connection with their support medium is achieved through a non-tensile interface where the shear forces are frictional. Examples of rocking systems can be found in a wide range of applications: from museum exhibits and hospital equipment to electrical devices and structural elements. The response of such systems when subjected to ground excitations is substantially different than components with moment connections. A distinctive feature is the appearance of rigid body rotations and displacements during the motion. These are often dominant and hence the criteria of failure of such bodies are mainly kinematic, rather than the usual stress exceedance criteria used for typical structural systems.

As a reasonable consequence, the majority of relevant literature examines rocking systems under the assumptions of rigid support medium and body (Housner 1963), or by assuming that the rocking body is flexible only in the lateral direction (Acikgoz and DeJong 2012). However, the decelerations of the rocking body during the occurring impacts are often of the order of tenths of g. These large forces may induce large local stresses at the points of application that may deteriorate the contact surface or lead to local failures.

The previous mode of failure has often been ignored in the literature. This is mainly due to the computational complexity of the problem that lays in between large displacement kinematics and computational mechanics. The change of the contact surface during the rocking motion in combination with an impact and sliding contact problem pose substantial challenges for standard FE methods: they result in the need of re-meshing techniques, or very dense initial meshes. The latter solution in turn

[1]Ph.D. candidate, Dept. of Civil Engineering, Univ. of Nottingham, Nottingham, NG7 2RD, UK, evxek3@nottingham.ac.uk
[2]Associate Professor, Dept. of Engineering Science, Univ. of Oxford, Oxford, OXI 3PA, UK, chatzis@eng.ox.ac.uk
[3]Assistant Professor, Dept. of Civil Engineering, Univ. of Nottingham, Nottingham, NG7 2RD, UK, savvas.triantafyllou@nottingham.ac.uk

results in further increased demands from the time integration method used so as to ensure stability. Such an approach could potentially lead to the deceiving result that the underlying physical problem is chaotic, when in reality the issue often lies in the robustness of the computational treatment. Furthermore, mesh distortion errors that are inevitable in large kinematics finite element analyses hinder the fidelity of rocking body simulations where the deformability of the contact surfaces significantly affects the resulting contact forces.

Recently, particle in cell methods and most notably material point methods have been found to provide solution of high fidelity for problems pertaining to large displacement and large deformations (Sulsky et al. (1994)). Rather than relying on the notion of a deforming mesh, material point methods introduce a particle based approximation for the deformable body. Contrary to purely particle based methods however, particles in Material Point Methods are mapped onto a non-deforming Eulerian mesh where solution of the governing equations is performed. This introduces a considerable advantage as opposed to purely particle based methods as the continuum approximation is preserved thus releasing the requirement for high particle densities. Hence, Material Point Methods retain the accuracy of particle based methods but avoid their increased computational costs.

To alleviate the previous problems and develop rocking models that allow the study of the stresses induced in rocking systems the authors propose the use of a Material Point Method (MPM) for simulating the rocking kinematics of deformable bodies. In this paper, the developed model is used to study the dynamics of a relatively stiff body and support medium and the solutions obtained are compared versus existing models in the literature.

2. RIGID BODY ROCKING MODELS

The Inverted Pendulum Model (IPM), developed by Housner (1963), is potentially the most popular model for rocking bodies. The rocking body, the properties and the axes convention used in the following equations are defined in Figure 1. The rigid body is defined by its mass m, half-width and half-height b and h, respectively. The occurring moment of inertia, about any of the bottom corners 0 and $0'$, is denoted as I_0 whereas $R = \sqrt{h^2 + b^2}$ stands for the distance from a corner to the center of mass and the angle $a = \tan^{-1} b/h$ describes the slenderness of the block.

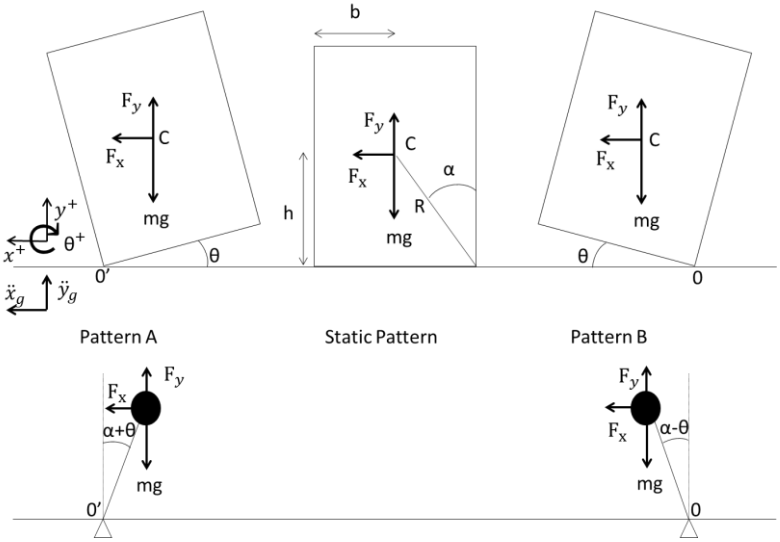

Figure 1. Inverted Pendulum Model (IPM defined by Housner (1963) for a free-standing rocking block.

The body rocks with respect to one of the corners depending on the sign of θ. Thus, it can be simulated by a pendulum whose pin is located at that corner as shown in Figure 1. This further implies that the body is assumed to not slide, or experience free-flight, that the body and the ground are rigid, and that the response of the body is strictly planar.

When θ transitions through zero an impact occurs between the body and the ground and as a result, the body may lose kinetic energy as it transitions, accordingly, from one pendulum pattern to the other. If it is further assumed that the angular momentum with respect to the future rocking corner is conserved, the reduction of energy factor, r, which relates the kinetic energy before and after impact is expressed as

$$r = \frac{\left(\dot{\theta}^{+}\right)^2}{\left(\dot{\theta}^{-}\right)^2} = \frac{1/2 I_0 \dot{\theta}_2^2}{1/2 I_0 \dot{\theta}_1^2} = \left[1 - \frac{mR^2}{I_0}\left(1 - \cos(2a)\right)\right]^2 \tag{1}$$

where $\dot{\theta}^{+}$ and $\dot{\theta}^{-}$ are the angular velocity after and before impact respectively. Hence, the IPM results in a discontinuity of the velocity state before and after the impact. It should further be noted that as discussed in Chatzis et al. (2017), the reduction of energy factor could well be within the value defined in equation (1) and unity, i.e., no loss of energy during impacts. To be able to alleviate that related uncertainty the contact interface mechanics have to be specified.

A means of achieving that while also introducing the deformability of the support medium is through the Winkler Model (WM) proposed in Chatzis and Smyth (2012a) for rocking bodies with a flat base. The model is illustrated in the following Figure 2

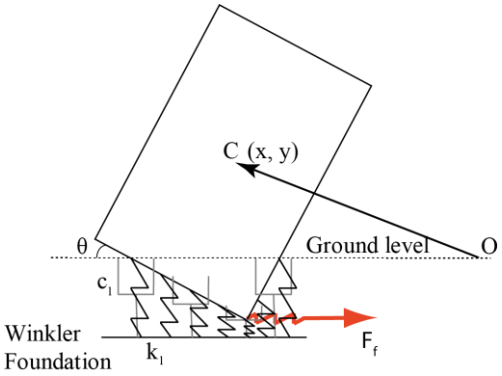

Figure 2. WM for rocking bodies on deformable media

The support medium parameters used in the model are the distributed per unit length stiffness k_l and damping coefficients c_l, while nonlinear horizontal springs are used for the frictional forces F_f. A Coulomb friction model is used that is defined by the coefficient of friction μ_f. The motion of the rigid body is described by the horizontal, vertical and rotational generalized coordinates (x, y and θ respectively in the paper). As a result, the model allows for including the effects of impact, sliding and free flight without discontinuities in the states. Additionally, no assumption needs to be made regarding the impact duration as the dissipated energy is a parameter of the WM properties.

3. MATERIAL POINT METHOD FOR CONTACT DYNAMICS

3.1 Strong form

An arbitrary deformable domain Ω is considered herein with external boundary $\partial\Omega$. It is assumed that the domain Ω consists of two deformable bodies, termed discrete fields, i.e., Ω_1 and Ω_2 so that $\Omega_1 \cup \Omega_2 = \Omega$. At time t, the two discrete fields are considered to be in contact along the surface $\partial\Omega_{\bar{f}}$ as shown in Figure 3(a). The strong form of this contact problem together with the corresponding boundary and initial conditions is presented in equations (2) below

$$\nabla \cdot \boldsymbol{\sigma} + \boldsymbol{b} = \rho\, \ddot{\boldsymbol{u}} \quad \text{on } \Omega \quad \text{(a)}$$
$$\boldsymbol{\sigma} \cdot \boldsymbol{n} = \bar{\boldsymbol{t}} \quad \text{on } \partial\Omega_{\bar{t}} \quad \text{(b)}$$
$$\boldsymbol{u} = \bar{\boldsymbol{u}} \quad \text{on } \partial\Omega_{\bar{u}} \quad \text{(c)} \qquad (2)$$

$$\boldsymbol{u} = {}^{(0)}\boldsymbol{u} \quad , \quad \dot{\boldsymbol{u}} = {}^{(0)}\dot{\boldsymbol{u}} \quad , \quad \ddot{\boldsymbol{u}} = {}^{(0)}\ddot{\boldsymbol{u}} \qquad \text{on } {}^{(0)}\Omega \qquad \text{(d)}$$
$$\boldsymbol{\sigma}_1 \cdot \boldsymbol{n}_1^{cont} = \bar{\boldsymbol{f}}_1^{cont} \quad , \quad \boldsymbol{\sigma}_2 \cdot \boldsymbol{n}_2^{cont} = \bar{\boldsymbol{f}}_2^{cont} \qquad \text{on } \partial\Omega_{\bar{f}} \qquad \text{(e)}$$

where $\boldsymbol{\sigma}$, $\boldsymbol{b}$ are the stress field and body forces, ρ is the mass density of domain Ω whereas $\boldsymbol{u}$, $\dot{\boldsymbol{u}}$ and $\ddot{\boldsymbol{u}}$ are the displacement, velocity and acceleration field respectively. Furthermore, it is assumed that traction/pressure forces $\bar{\boldsymbol{t}}$ are applied on $\partial\Omega_{\bar{t}}$ while $\bar{\boldsymbol{u}}$ and $\boldsymbol{n}$ stands for the prescribed displacement field on $\partial\Omega_{\bar{u}}$ and the outward unit normal vector of the boundary $\partial\Omega$ respectively. When the two bodies are in contact, a contact force $\bar{\boldsymbol{f}}^{cont}$ is also acting on them. In particular, the contact force

$$\bar{\boldsymbol{f}}_1^{cont} = \bar{\boldsymbol{f}}_1^{nor} + \bar{\boldsymbol{f}}_1^{tan} = \bar{f}_1^{nor} \cdot \boldsymbol{n}_1^{cont} + \bar{f}_1^{tan} \cdot \boldsymbol{s}_1^{cont}$$

is applied on Ω_1 from Ω_2 whereas definition of $\bar{\boldsymbol{f}}_2^{cont}$ is derived accordingly. These contact forces satisfy the boundary conditions (2e) along $\partial\Omega_{\bar{f}}$ where $\boldsymbol{\sigma}_1$, $\boldsymbol{n}_1^{cont}$ and $\boldsymbol{s}_1^{cont}$ are the stress field, the outward unit normal and tangential vector of body Ω_1 (similarly for $\boldsymbol{\sigma}_2$ and $\boldsymbol{n}_2^{cont}$) respectively. Additionally, the strong form is supplemented by the kinematic constrains shown below, i.e.

$$\boldsymbol{n}_1^{cont} = -\boldsymbol{n}_2^{cont} \quad , \quad \boldsymbol{s}_1^{cont} = -\boldsymbol{s}_2^{cont} \qquad \text{Collinearity} \qquad \text{(a)}$$
$$\bar{\boldsymbol{f}}_1^{nor} = -\bar{\boldsymbol{f}}_2^{nor} \quad , \quad \bar{\boldsymbol{f}}_1^{tan} = -\bar{\boldsymbol{f}}_2^{tan} \qquad \text{(b)}$$
$$\bar{f}^{nor} \leq 0 \qquad \text{Non-tension} \qquad \text{(c)}$$
$$\gamma_n \leq 0 \qquad \text{Impenetrability} \qquad \text{on } \partial\Omega_{\bar{f}} \qquad \text{(d)} \qquad (3)$$
$$\gamma_n \bar{f}^{nor} = 0 \qquad \text{Complementarity (normal)} \qquad \text{(e)}$$
$$\left|\bar{f}^{tan}\right| \leq \mu_f \left|\bar{f}^{nor}\right| \qquad \text{Coulomb friction model} \qquad \text{(f)}$$
$$|\gamma_s| \geq 0 \qquad \text{Slip/No-slip} \qquad \text{(g)}$$
$$|\gamma_s|\left(\left|\bar{f}^{tan}\right| - \mu_f \left|\bar{f}^{nor}\right|\right) = 0 \qquad \text{Complementarity (tangential)} \qquad \text{(h)}$$

where

$$\gamma_n = (\dot{\boldsymbol{u}}_1 - \dot{\boldsymbol{u}}_2) \cdot \boldsymbol{n}_1^{cont} = (\dot{\boldsymbol{u}}_2 - \dot{\boldsymbol{u}}_1) \cdot \boldsymbol{n}_2^{cont} \qquad \gamma_s = (\dot{\boldsymbol{u}}_1 - \dot{\boldsymbol{u}}_2) \cdot \boldsymbol{s}_1^{cont} = (\dot{\boldsymbol{u}}_2 - \dot{\boldsymbol{u}}_1) \cdot \boldsymbol{s}_2^{cont}$$

and μ_f stands for the friction coefficient. These kinematic constrains are imposed on $\partial\Omega_{\bar{f}}$ to satisfy collinearity, impenetrability, and non-tension as well as to account for slip or stick conditions (according to Coulomb friction model) between the two bodies.

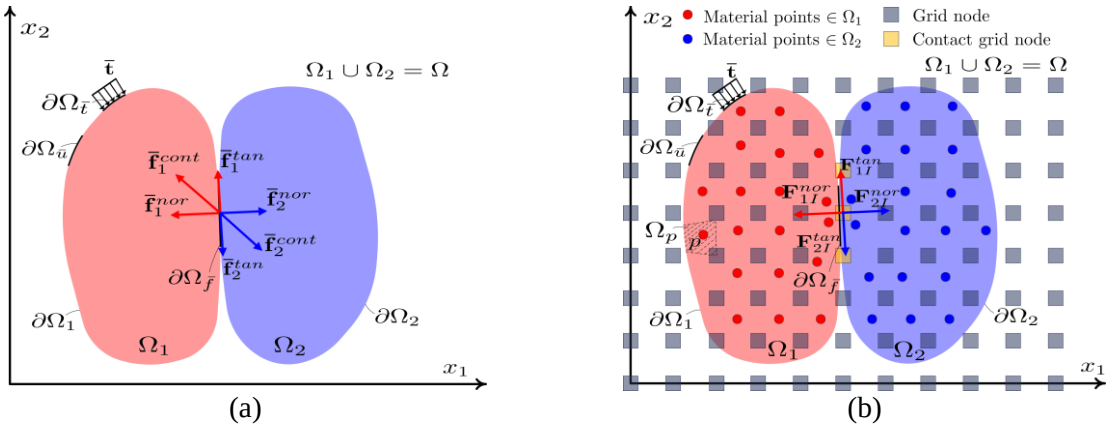

Figure 3. (a) Continuum bodies (discrete fields) into contact (b) Material Point Method approximation

3.2 Numerical Implementation

In material point method, the continuum is discretised into a set of N_p material points (integration points) that are moving within a fixed Eulerian Grid. The Eulerian Grid is discretised into a set of N_c

grid cells and corresponding grid nodes N_n where the equations of motion are solved (see also Figure 3(b)). This grid is a non-deforming mesh where all the material points quantities are mapped into utilizing appropriate interpolation functions. Based on this discretization, both the mass density ρ_b and domain volume Ω_b are additively decomposed for each discrete field b where $b = 1,2$ into

$$\rho_b(\boldsymbol{x}_b, t) = \sum_{p=1}^{N_p} \rho_{bp}\Omega_{bp}\,\delta(\boldsymbol{x}_b - \boldsymbol{x}_{bp}) \quad \text{(a)} \qquad \Omega_b(\boldsymbol{x}_b, t) = \sum_{p=1}^{N_p} \Omega_{bp}\,\delta(\boldsymbol{x}_b - \boldsymbol{x}_{bp}) \quad \text{(b)} \quad (4)$$

respectively, where denotes δ the Dirac function. All the quantities with the subscript p are referred to the p^{th} material point corresponding quantities. Employing Galerkin approximation (Hughes, 2012) and defining appropriate trial solution and weighting spaces as

$$\mathrm{S} = \{\boldsymbol{u} \in H_1(\Omega) | \, \boldsymbol{u} = \bar{\boldsymbol{u}}, \partial\Omega_{\bar{u}}\} \qquad \mathrm{\mathfrak{D}} = \{\boldsymbol{w} \in H_1(\Omega) | \, \boldsymbol{w} = 0, \partial\Omega_{\bar{u}}\}$$

for the displacement field $\boldsymbol{u}$ and weighting field $\boldsymbol{w}$ respectively, the strong form of equation (2) is cast into the following weak form

$$\begin{aligned}\int_{\Omega_b} (\rho_b \ddot{\boldsymbol{u}}_b \cdot \boldsymbol{w}_b)\, d\Omega_b + \int_{\Omega_b} (\boldsymbol{\sigma}_b : \nabla \boldsymbol{w}_b)\, d\Omega_b \\ = \int_{\Omega_b} (\boldsymbol{b}_b \cdot \boldsymbol{w}_b)\, d\Omega_b + \int_{\partial\Omega_{b\bar{t}}} (\bar{\boldsymbol{t}}_b \cdot \boldsymbol{w}_b)\, d\partial\Omega_{b\bar{t}} + \int_{\partial\Omega_{b\bar{f}}} (\bar{\boldsymbol{f}}_b^{cont} \cdot \boldsymbol{w}_b)\, d\partial\Omega_{b\bar{f}}\end{aligned} \quad (5)$$

By further utilizing equations (4a) and (4b) respectively, the following discrete equation is established

$$\begin{aligned}\sum_{p=1}^{N_p} (\rho_{bp} \ddot{\boldsymbol{u}}_{bp} \cdot \boldsymbol{w}_{bp}\, \Omega_{bp}) + \sum_{p=1}^{N_p} (\boldsymbol{\sigma}_{bp} : \nabla \boldsymbol{w}_{bp}\, \Omega_{bp}) = \sum_{p=1}^{N_p} (\boldsymbol{b}_{bp} \cdot \boldsymbol{w}_{bp}\, \Omega_{bp}) \\ = \int_{\partial\Omega_{b\bar{t}}} (\bar{\boldsymbol{t}}_b \cdot \boldsymbol{w}_b)\, d\partial\Omega_{b\bar{t}} + \int_{\partial\Omega_{b\bar{f}}} (\bar{\boldsymbol{f}}_b^{cont} \cdot \boldsymbol{w}_b)\, d\partial\Omega_{b\bar{f}}\end{aligned} \quad (6)$$

The displacement field $\boldsymbol{u}_{bp}$ **(**also $\dot{\boldsymbol{u}}_{bp}$ and $\ddot{\boldsymbol{u}}_{bp}$) and the weighting functions $\boldsymbol{w}_{bp}$ are interpolated at corresponding nodal values as

$$\boldsymbol{u}_{bp} = \sum_{p=1}^{N_n} (N_I(\boldsymbol{x}_{bp}) \cdot \boldsymbol{u}_{bI}) \quad \text{(a)} \qquad \boldsymbol{w}_{bp} = \sum_{p=1}^{N_n} (N_I(\boldsymbol{x}_{bp}) \cdot \boldsymbol{w}_{bI}) \quad \text{(b)} \quad (7)$$

where in this work, $N_I(\boldsymbol{x}_{bp})$ are higher-order B-spline interpolation (Hughes T.J.R. 2012) functions of node I evaluated at the material points $\boldsymbol{x}_{bp}$. After the necessary algebraic manipulations equation (6) is eventually cast in the following compact form at time t

$${}^{(t)}\boldsymbol{M}_{bI}^{u}\,{}^{(t)}\ddot{\boldsymbol{u}}_{bI} + {}^{(t)}\boldsymbol{F}_{bI}^{int} = {}^{(t)}\boldsymbol{F}_{bI}^{ext} + {}^{(t)}\boldsymbol{F}_{bI}^{cont} \quad (8)$$

where ${}^{(t)}\boldsymbol{F}_{bI}^{int}$ corresponds to the nodal components of the internal force vector at node I as

$${}^{(t)}\boldsymbol{F}_{bI}^{int} = \sum_{p=1}^{N_p} (\nabla N_I({}^{(t)}\boldsymbol{x}_{bp}) \cdot {}^{(t)}\boldsymbol{\sigma}_{bp}\, \Omega_{bp}) \quad (9)$$

whereas ${}^{(t)}\boldsymbol{F}_{bI}^{ext}$ is the component of the external force vector at node I

$$ {}^{(t)}\boldsymbol{F}_{bI}^{ext} = \sum_{p=1}^{N_p} \boldsymbol{b}_{bp}\, N_I\big({}^{(t)}\boldsymbol{x}_{bp}\big)\, \Omega_{bp} + \int_{\partial\Omega_{b\bar{t}}} \bar{\boldsymbol{t}}_b\, N_I\big({}^{(t)}\boldsymbol{x}_{bp}\big) d\partial\Omega_{b\bar{t}} \tag{10} $$

respectively. The lumped mass matrix ${}^{(t)}\boldsymbol{M}_{bI}^{u}$ is evaluated as

$$ {}^{(t)}\boldsymbol{M}_{bI}^{u} = \sum_{p=1}^{N_p} \rho_{bp}\, N_I\big({}^{(t)}\boldsymbol{x}_{bp}\big)\, \Omega_{bp} \tag{11} $$

Considering a forward Euler integration scheme, equation of motion (8) can be conveniently established in the following momentum form

$$ {}^{(t+\Delta t)}\boldsymbol{p}_{bI} = {}^{(t)}\boldsymbol{p}_{bI} + \Delta t\big({}^{(t)}\boldsymbol{F}_{bI}^{ext} + {}^{(t)}\boldsymbol{F}_{bI}^{cont} - {}^{(t)}\boldsymbol{F}_{bI}^{int}\big) \tag{12} $$

where ${}^{(t)}\boldsymbol{p}_{bI}$ corresponds to the momentum of the discrete field at time t. This is projected from the material points to the computational grid through equation (13)

$$ {}^{(t)}\boldsymbol{p}_{bI} = \sum_{p=1}^{N_p} \big(N_I\big({}^{(t)}\boldsymbol{x}_{bp}\big) M_{bp}\, {}^{(t)}\dot{\boldsymbol{u}}_{bp}\big) \tag{13} $$

In this work, equation (12) is numerically solved using a predictor-corrector algorithm introduced by Bardenhagen S. et al. (2000) and further improved by Huang P. et al. (2010). In this, the trial momentums are initially evaluated, neglecting the contact forces, as

$$ {}^{(t+\Delta t)}\boldsymbol{p}_{bI}^{trl} = {}^{(t)}\boldsymbol{p}_{bI} + \Delta t\big({}^{(t)}\boldsymbol{F}_{bI}^{ext} - {}^{(t)}\boldsymbol{F}_{bI}^{int}\big) \tag{14} $$

The corresponding trial nodal velocities are computed accordingly as

$$ {}^{(t+\Delta t)}\dot{\boldsymbol{u}}_{bI}^{trl} = \frac{{}^{(t+\Delta t)}\boldsymbol{p}_{bI}^{trl}}{{}^{(t)}\boldsymbol{M}_{bI}^{u}} \tag{15} $$

and correspond to the velocities of each discrete field b when no contact force is exerted between them. The nodal centre of mass velocities are calculated using equation (16) below

$$ {}^{(t+\Delta t)}\dot{\boldsymbol{u}}_{I}^{cm} = \frac{\sum_{b=1}^{2} {}^{(t+\Delta t)}\boldsymbol{p}_{bI}^{trl}}{\sum_{b=1}^{2} {}^{(t)}\boldsymbol{M}_{bI}^{u}} \tag{16} $$

These correspond to the velocities that each discrete field b would have if these were to move a single field (non-slip contact). Using equations (15) and (16) the normal component of contact force is expressed as

$$ {}^{(t)}F_{bI}^{nor,s} = \frac{{}^{(t)}M_{bI}^{u}}{\Delta t}\big({}^{(t+\Delta t)}\dot{\boldsymbol{u}}_{bI}^{cm} - {}^{(t+\Delta t)}\dot{\boldsymbol{u}}_{bI}^{trl}\big) \cdot {}^{(t)}\boldsymbol{n}_{bI}^{cont} \tag{17} $$

where the surface unit normal vector is computed as

$$ {}^{(t)}\boldsymbol{n}_{1I}^{cont} = -\,{}^{(t)}\boldsymbol{n}_{2I}^{cont} = \frac{{}^{(t)}\widehat{\boldsymbol{n}}_{1I}^{cont} - {}^{(t)}\widehat{\boldsymbol{n}}_{2I}^{cont}}{\big\|{}^{(t)}\widehat{\boldsymbol{n}}_{1I}^{cont} - {}^{(t)}\widehat{\boldsymbol{n}}_{2I}^{cont}\big\|} \tag{18} $$

where

$$ {}^{(t)}\hat{\boldsymbol{n}}_{bI}^{cont} = \frac{\sum_{p=1}^{N_p} \nabla N_I\left({}^{(t)}\boldsymbol{x}_{bp}\right) M_{bp}}{\left\| \sum_{p=1}^{N_p} \nabla N_I\left({}^{(t)}\boldsymbol{x}_{bp}\right) M_{bp} \right\|} \tag{19} $$

To satisfy the non-tensional constrain during contact, the normal component should be modified as

$$ {}^{(t)}F_{bI}^{nor} = \min\left(0, {}^{(t)}F_{bI}^{nor,s}\right) \tag{20} $$

Similarly, the tangential component of contact force is computed as

$$ {}^{(t)}F_{bI}^{tan,s} = \frac{{}^{(t)}M_{bI}^{u}}{\Delta t}\left({}^{(t+\Delta t)}\dot{\boldsymbol{u}}_{bI}^{cm} - {}^{(t+\Delta t)}\dot{\boldsymbol{u}}_{bI}^{trl}\right) \cdot {}^{(t)}\boldsymbol{s}_{bI}^{cont} \tag{21} $$

where the surface unit tangential vector ${}^{(t)}\boldsymbol{s}_{bI}^{cont}$ can be derived as the unit vector that forms an orthogonal basis with ${}^{(t)}\boldsymbol{n}_{bI}^{cont}$. The tangential component can be further modified, considering the Coulomb friction model, as

$$ {}^{(t)}F_{bI}^{tan} = \min\left(\mu_f \left|{}^{(t)}F_{bI}^{nor}\right|, \left|{}^{(t)}F_{bI}^{tan,s}\right|\right) \operatorname{sign}\left({}^{(t)}F_{bI}^{tan,s}\right) \tag{22} $$

Therefore, the contact force is eventually evaluated as

$$ {}^{(t)}\boldsymbol{F}_{bI}^{cont} = {}^{(t)}F_{bI}^{nor} \cdot {}^{(t)}\boldsymbol{n}_{bI}^{cont} + {}^{(t)}F_{bI}^{tan} \cdot {}^{(t)}\boldsymbol{s}_{bI}^{cont} \tag{23} $$

when the impenetrability condition $\left({}^{(t+\Delta t)}\dot{\boldsymbol{u}}_{bI}^{trl} - {}^{(t+\Delta t)}\dot{\boldsymbol{u}}_{bI}^{cm}\right) \cdot {}^{(t)}\boldsymbol{n}_{bI}^{cont} > 0$ is satisfied at contact nodes. To account for the true velocities, the initially predicted trial velocities ${}^{(t+\Delta t)}\dot{\boldsymbol{u}}_{bI}^{trl}$ introduced in equation (15) should be corrected according to the following relation

$$ {}^{(t+\Delta t)}\dot{\boldsymbol{u}}_{bp} = {}^{(t+\Delta t)}\dot{\boldsymbol{u}}_{bI}^{trl} + \Delta t \frac{{}^{(t)}\boldsymbol{F}_{bI}^{cont}}{{}^{(t)}\boldsymbol{M}_{bI}^{u}} \tag{24} $$

Once the velocities ${}^{(t+\Delta t)}\dot{\boldsymbol{u}}_{bp}$ are computed, the total strains at p^{th} material point can be evaluated as

$$ {}^{(t+\Delta t)}\boldsymbol{\varepsilon}_{bp} = {}^{(t)}\boldsymbol{\varepsilon}_{bp} + \frac{1}{2}\Delta t \sum_{I=1}^{N_n} \left(\nabla N_I\left({}^{(t)}\boldsymbol{x}_{bp}\right){}^{(t+\Delta t)}\dot{\boldsymbol{u}}_{bI} + \left(\nabla N_I\left({}^{(t)}\boldsymbol{x}_{bp}\right){}^{(t+\Delta t)}\dot{\boldsymbol{u}}_{bI}\right)^T\right) \tag{25} $$

while the total stresses from the relation below

$$ {}^{(t+\Delta t)}\boldsymbol{\sigma}_{bp} = D_{bp}\,{}^{(t+\Delta t)}\boldsymbol{\varepsilon}_{bp} \tag{26} $$

where D_{bp} stands for the constitutive matrix. Finally, the displacement, velocity and acceleration field of p^{th} material point are updated as

$$ {}^{(t+\Delta t)}\boldsymbol{u}_{bp} = {}^{(t)}\boldsymbol{u}_{bp} + \Delta t \sum_{I=1}^{N_n} \left(N_I\left({}^{(t)}\boldsymbol{x}_{bp}\right){}^{(t+\Delta t)}\dot{\boldsymbol{u}}_{bI}\right) \tag{27} $$

$$ {}^{(t+\Delta t)}\dot{\boldsymbol{u}}_{bp} = {}^{(t)}\dot{\boldsymbol{u}}_{bp} + \Delta t \sum_{I=1}^{N_n} \left(N_I\left({}^{(t)}\boldsymbol{x}_{bp}\right)\frac{{}^{(t)}\boldsymbol{F}_{bI}^{ext} + {}^{(t)}\boldsymbol{F}_{bI}^{cont} - {}^{(t)}\boldsymbol{F}_{bI}^{int}}{{}^{(t)}\boldsymbol{M}_{bI}^{u}}\right) \tag{28} $$

and

$$ {}^{(t)}\ddot{\boldsymbol{u}}_{bp} = \sum_{I=1}^{N_n} \left(N_I\left({}^{(t)}\boldsymbol{x}_{bp}\right) \frac{{}^{(t)}\boldsymbol{F}_{bI}^{ext} + {}^{(t)}\boldsymbol{F}_{bI}^{cont} - {}^{(t)}\boldsymbol{F}_{bI}^{int}}{{}^{(t)}\boldsymbol{M}_{bI}^{u}} \right) \tag{29} $$

respectively. The material point position is hence updated according to the following relation

$$ {}^{(t+\Delta t)}\boldsymbol{x}_{bp} = {}^{(t)}\boldsymbol{x}_{bp} + \Delta t \sum_{I=1}^{N_n} \left(N_I\left({}^{(t)}\boldsymbol{x}_{bp}\right) {}^{(t+\Delta t)}\dot{\boldsymbol{u}}_{bI} \right) \tag{30} $$

leading to formulation that explicitly and accurately accounts for large displacement kinematics without mesh distortion as the latter remains undeformed.

4. NUMERICAL RESULTS

The rocking response of a body with dimensions $2b = 0.795$ m and $2h = 3.113$ m, shown in Figure 4(a) resting on an elastic medium is simulated herein using the proposed MPM scheme. The body is subjected to a horizontal ground acceleration prescribed by a single sinusoidal pulse defined in equation (31) as

$$ \ddot{u}_g = \begin{cases} a \sin(\omega\, t)\,, & 0 \le t < \dfrac{2\pi}{\omega} \\ 0, & t \ge \dfrac{2\pi}{\omega} \end{cases} \tag{31} $$

where a and ω are the amplitude and the frequency of the excitation respectively. The Young's modulus and Poisson ratio of the ground are $E = 260$ MPa and $v = 0.30$ respectively. The corresponding parameters for the body are chosen as $E = 5200$ MPa and $v = 0.30$. The parameters were chosen so that the body is substantially more rigid than the support medium. This allows for comparison versus previous work in the literature as the dimensions of the specific body under the assumption of it being rigid have been used in the works of Zhang and Makris (2001) and Chatzis and Smyth (2012a & 2012b). The mass density of the ground is $\rho = 1300$ kg/m^3 whereas the mass density of the rigid body is $\rho = 606.101$ kg/m^3. The latter allows for comparing versus the mass per unit length used for this body in Chatzis and Smyth (2012a). The friction coefficient between the rocking body and the ground is $\mu_f = 0.625$.

According to the MPM formulation introduced in Section 3 two discrete fields are considered; one corresponding to the rigid body and one corresponding to the elastic medium. The former is discretized into 8928 material points whereas 7200 material points are used for the latter. Quadratic b-splines are utilized for the background grid with cell spacing 0.05 m and plane strain conditions are assumed. Initially, the material points are positioned in the Gauss positions of each parent cell; the cell density is 3x3. A time step $\Delta t = 0.00001$ sec is employed. The ground excitation is applied to MPM model employing D' Alembert's principle.

As has been initially shown in Zhang and Makris (2001), utilizing the IPM, the outcome of the body, in terms of survival or toppling, when subjected to single cycle acceleration pulses of varying frequency and amplitude (ω, a) offers useful information on the stability of the system. By varying the values of ω and a in the horizontal and vertical axes respectively and by denoting for a given frequency the amplitudes at which a transition between survival and failure is observed the stability diagram of Figure 4(b) can be generated. In such a diagram, three distinct regions can be observed: a region of survival, a closed region (loop) where the body topples having experienced a single impact with the ground, and an area of failure occurring for larger amplitudes where the body fails without having experienced an impact. The boundaries between those regions for the IPM are indicated in Figure 4(b) with a magenta hexagram. Using a deformable WM for the support medium, for the same

body Chatzis and Smyth (2012a) produced a stability diagram which also included the presence of the three regions. The WM predicted boundaries are also plotted in Figure 4(b) with a golden square.

A set of 127 analyses is carried out with various pairs of (ω, a) to derive the stability diagram of Figure 4(b). The axes are normalized as ω/p and a/a_g respectively, where $p = 2.14$ and $a_g = 2.5049$. In this work green dots, blue pentagrams and red diamonds correspond to the result obtained from the proposed MPM model and account for safe, failure with impact and failure without impact respectively. It should be noted the body is considered to survive, after experiencing two impacts without failure during its free vibration response. The body is considered to fail when $|\theta| > 85^o$ where θ is the angle between the rocking body and the ground. The obtained results are superimposed on the boundaries predicted by the IPM and WM models.

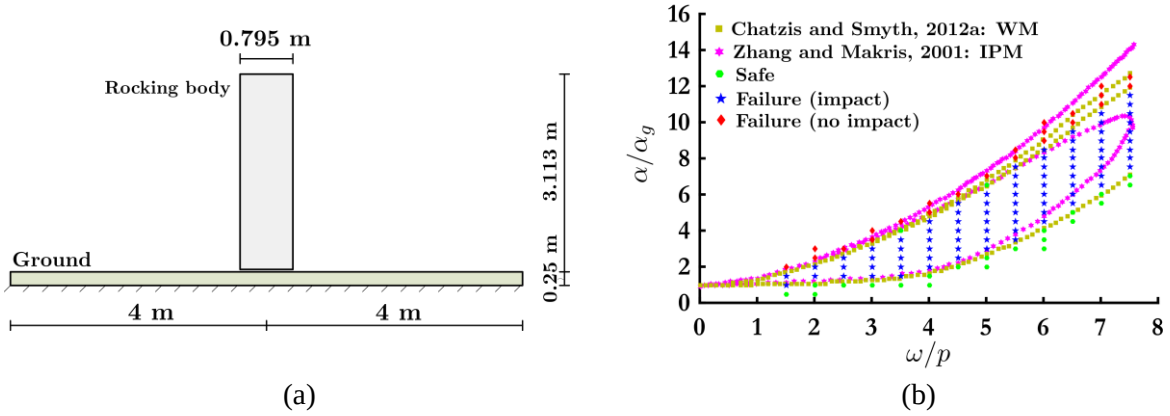

(a) (b)

Figure 4. (a) Geometry and boundary conditions (b) Failure-safety analysis with the WM, IPM and MPM.

As shown in Figure 4(b), the proposed MPM method demonstrates a very good agreement with WM. The two methods predict that the failure with no impact regions extends to larger frequencies than those predicted by the IPM model under the assumption of conserving angular moment with respect to the future rocking corner. This phenomenon has been further explained in Chatzis et al. (2017) where it is argued that bodies with a flat base would not necessarily satisfy this assumption. Similarly to the WM, MPM does not need to adopt such an assumption, but rather relies on modeling the properties of the bodies in contact and accurately resolving the corresponding contact interfaces. It is further expected that the MPM model would show a better agreement to the results in Zhang and Makris (2001) if the same body had feet on the two corners, similarly to what has been demonstrated in Chatzis and Smyth (2012a) for the Concentrated Spring Model (CSM).

It should further be stated that the stability diagram for the WM shown in Chatzis and Smyth (2012a) and in Figure 4(b) uses an estimate of the properties on the contact interface stiffness and damping based on the model of Wolf (1994), which essentially simulates the support medium as an elastic half-space. It further appears that this model is also reasonable for the case studied here. However, the MPM does not need to make an assumption on the contact interface properties which is a further advantage of the model presented herein.

In the following, three individual cases are presented for each failure-safety condition. In the first case, the pair $\omega/p = 3$, $a/a_g = 1$ results in survival for the rocking body. A snapshot of the response of the rocking body is presented in Figure 5 at chosen time instances. The ground excitation and rocking body angle time histories are presented in Figure 6. In the second case, the frequency is the same ratio $\omega/p = 3$ is considered while the amplitude is increased to $a/a_g = 2.5$. That pair leads the rocking body to toppling after having experience one impact with the ground. The complete rocking response is represented in Figure 7. Similarly, the ground excitation and rocking angle time-histories are shown in Figure 8.

In the third case, the amplitude is increased to $a/a_g = 3.5$. This amplitude seems to be adequate to

overturn the rocking body without impact. The corresponding rocking motion is presented in Figure 9 whereas the ground excitation time-history and corresponding rocking angle are shown in Figure 10.

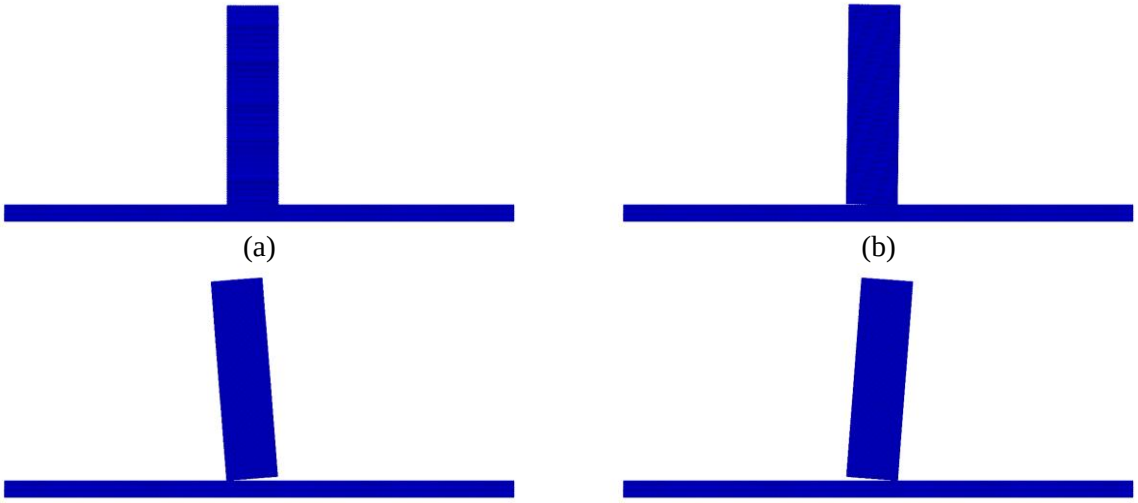

(a) (b)

(c) (d)

Figure 5. $\omega/p = 3$ and $a/a_g = 1$ (Safe): Rocking body response for (a) 0 sec (b) 0.47 sec (c) 1.20 sec and (d) 2.10 sec.

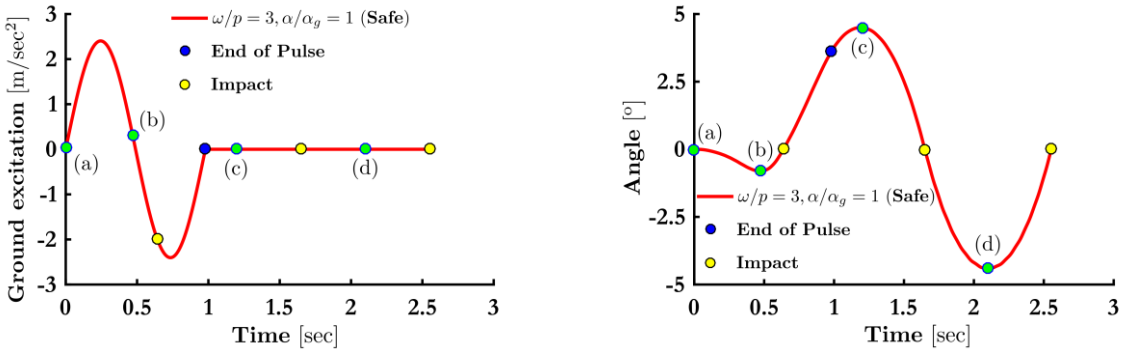

(a) (b)

Figure 6. $\omega/p = 3$ and $a/a_g = 1$ (Safe): Plots over time for (a) ground excitation (acceleration pulse) (b) rocking body angle with ground [labels a, b, c, d correspond to Figure 5 sub-captions].

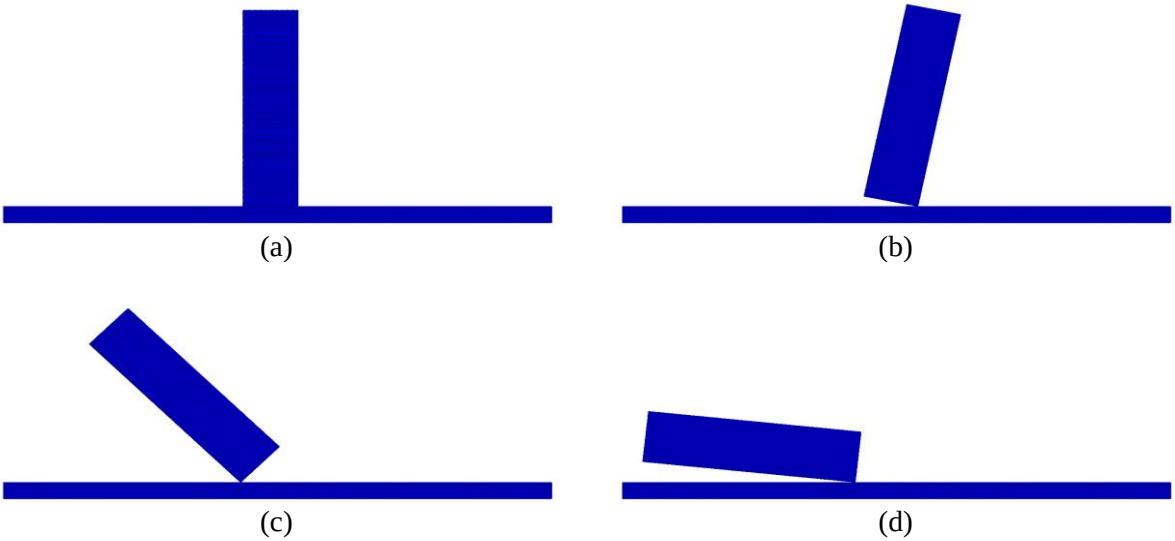

(a) (b)

(c) (d)

Figure 7. $\omega/p = 3$ and $a/a_g = 2.5$ (Failure (impact)): Rocking body response for (a) 0 sec (b) 0.73 sec (c) 2.51 sec and (d) 2.90 sec.

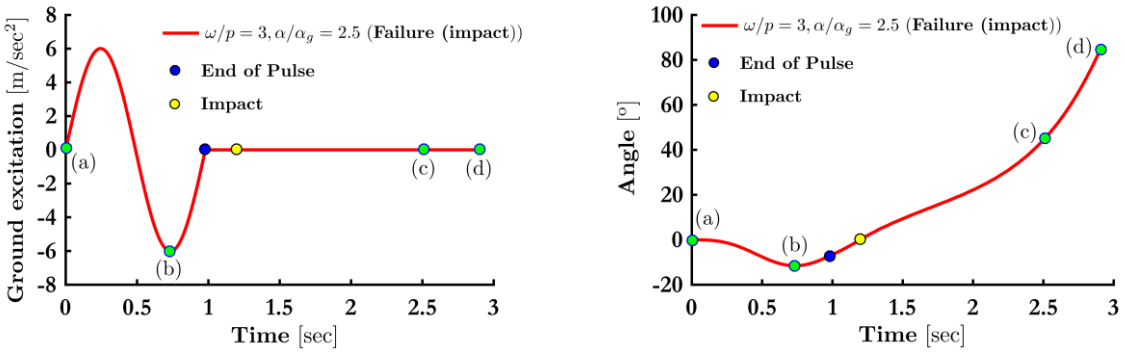

(a) (b)

Figure 8. $\omega/p = 3$ and $a/a_g = 2.5$ (Failure (impact)): Plots over time for (a) ground excitation (acceleration pulse) (b) rocking body angle with ground [labels a, b, c, d correspond to Figure 7 sub-captions].

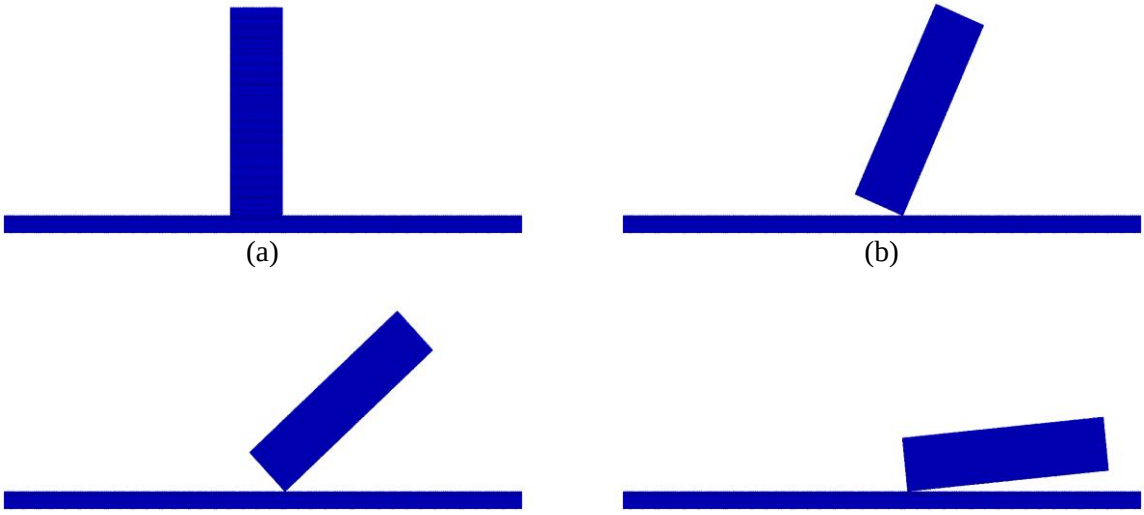

(a) (b)

(c) (d)

Figure 9. $\omega/p = 3$ and $a/a_g = 3.5$ (Failure (no impact)): Rocking body response for (a) 0 sec (b) 1.50 sec (c) 2.20 sec and (d) 2.58 sec.

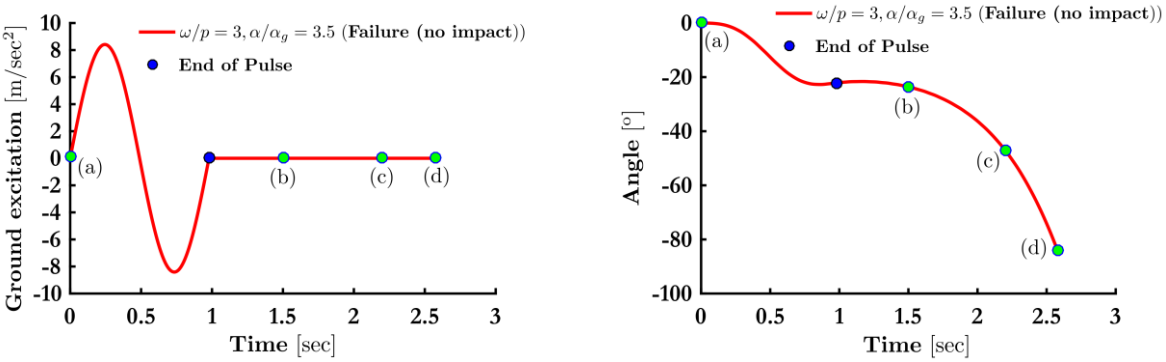

(a) (b)

Figure 10. $\omega/p = 3$ and $a/a_g = 3.5$ (Failure (no impact)): Plots over time for (a) ground excitation (acceleration pulse) (b) rocking body angle with ground [labels a, b, c, d correspond to Figure 9 sub-captions].

5. CONCLUSIONS

A material point method is presented for the simulation of rocking body dynamics. The method is rigorously established within a discrete field setting. In this, solution of the governing equations of motion is performed for each field individually while contact conditions between fields are explicitly

introduced into the strong form of the problem through appropriate boundary conditions. Solution of the resulting governing equations is performed in an explicit manner using a predictor corrector algorithm.

Results obtained with the proposed numerical for the case of a rigid body over an elastic half-space are compared against the Inverted Pendulum and Winkler rocking models. Results indicate that the numerical predictions are in good agreement with the estimates of both the Inverted Pendulum Model and the Winkler Model. As no assumption needs to be implied on either the stiffness of the rocking body or the contact interface properties, the proposed method provides an attractive alternative for the simulation of more complex problems, e.g., rocking of deformable and non-elastic bodies.

6. ACKNOWLEDGMENTS

This research has been partially supported by the University of Nottingham through the Dean of Engineering Prize, a scheme for pump priming support for early-career academic staff. The authors are grateful to the University of Nottingham for access to its High Performance Computing facility.

7. REFERENCES

Housner G.W. (1963). The behavior of inverted pendulum structures during earthquakes. *Bull. Seismol. Soc. Am., 53(2) , 403-417*.

Acikgoz S. and DeJong M. (2012). The interaction of elasticity and rocking in flexible structures allowed to uplift, Earthquake Engineering and Structural Dynamics, 41 (15), pp 2177-2194

Sulsky D., Chen Z. and Schreyer H.L. (1994). A particle method for history-dependent materials. *Computer Methods in Applied Mechanics and Engineering*, 118 (1-2), pp. 179-196

Bardenhagen S.G., Brackbill J.U. and Sulsky D. (2000). The material point method for granular materials. *Computer Methods in Applied Mechanics and Engineering*, 187: 529-541.

Huang P., Zhang X., Ma S. and Huang X. (2010). Contact algorithms for the material point method in impact and penetration simulation. *International Journal for Numerical Methods in Engineering*, 85: 498-517.

Chatzis M.N. and Smyth A.W. (2012a). Robust Modeling of the Rocking Problem. *Journal of Engineering Mechanics*, 138(3): 247-262.

Chatzis M.N. and Smyth A.W. (2012b). Modeling of the 3D rocking problem. *International Journal of Non-Linear Mechanics*, 47(4): 85-98.

Zhang J. and Makris N. (2001). Rocking Response of Free-Standing Blocks under Cycloidal Pulses. *Journal of Engineering Mechanics*, 127(5): 473-483.

Chatzis M.N., Espinosa G.M. and Smyth A.W. (2017). Examining the Energy Loss in the Inverted Pendulum Model for Rocking Bodies. *Journal of Engineering Mechanics*, 143(5): 04017013.

Wolf J.P. (1994). Foundation Vibration Analysis Using Simple Physical Models. *Prentice Hall, Upper Saddle River, NJ*.

Hughes T.J.R. (2012). The Finite Element Method: Linear Static and Dynamic Finite Element Method. *Courier Corporation*.